

Article

Comparative Study of MgO Nanopowders Prepared by Different Chemical Methods

Ligia Todan ^{1,†} , Luminița Predoană ^{1,†}, Gabriela Petcu ^{1,*}, Silviu Preda ^{1,*} , Daniela Cristina Culiță ¹ , Adriana Băran ¹, Roxana-Doina Trușcă ², Vasile-Adrian Surdu ² , Bogdan Ștefan Vasile ² , and Adelina-Carmen Ianculescu ²

¹ Institute of Physical Chemistry “Ilie Murgulescu” of the Romanian Academy, 202 Splaiul Independenței, 060021 Bucharest, Romania; adibaran@gmail.com (A.B.)

² Department of Science and Engineering of Oxide Materials and Nanomaterials, Faculty of Chemical Engineering and Biotechnologies, “Politehnica” University of Bucharest, 1-7 Gh. Polizu, 011061 Bucharest, Romania; adrian.surdu@upb.ro (V.-A.S.); bogdan.vasile@upb.ro (B.Ș.V.)

* Correspondence: gpetcu@icf.ro (G.P.); predas@icf.ro (S.P.)

† These authors contributed equally to this work.

Abstract: Magnesium oxide (MgO) was synthesized by three different methods: the sol–gel (SG), microwave-assisted sol–gel (MW), and hydrothermal (HT) methods for comparing the influence of the preparation conditions on the properties of the products. The powders were annealed at 450 °C. The samples were characterized by X-ray diffraction, scanning electron microscopy (SEM), transmission electron microscopy (TEM/HRTEM), selected area electron diffraction (SAED), energy-dispersive X-ray spectroscopy (EDX), BET specific surface area and porosity, photoluminescence, and UV–Vis spectroscopy. The samples consisted mainly of periclase as a crystalline phase, and the MW and HT preparation methods generated particles with higher specific surface areas. The powders had less-defined morphologies and high levels of aggregation. The optical band gaps of the samples were determined from UV DRS, and the photocatalytic activities of the magnesium oxides obtained by the three methods towards the degradation of methyl orange (MO) under UV light irradiation was evaluated.

Keywords: MgO nanopowders; sol–gel method; microwave-assisted sol–gel method; hydrothermal method; photocatalytic degradation of methyl orange dye



Citation: Todan, L.; Predoană, L.; Petcu, G.; Preda, S.; Culiță, D.C.; Băran, A.; Trușcă, R.-D.; Surdu, V.-A.; Vasile, B.Ș.; Ianculescu, A.-C. Comparative Study of MgO Nanopowders Prepared by Different Chemical Methods. *Gels* **2023**, *9*, 624. <https://doi.org/10.3390/gels9080624>

Academic Editor: Aris Giannakas

Received: 23 June 2023

Revised: 30 July 2023

Accepted: 31 July 2023

Published: 2 August 2023



Copyright: © 2023 by the authors. Licensee MDPI, Basel, Switzerland. This article is an open access article distributed under the terms and conditions of the Creative Commons Attribution (CC BY) license (<https://creativecommons.org/licenses/by/4.0/>).

1. Introduction

New and emerging fields of technology have provided materials prepared in the form of small particles with remarkable properties, such as being photocatalytic in nature, possessing a high surface area, being electrostatic, having a tunable pore volume, being magnetic, being hydrophobic and hydrophilic, etc., with novel potential applications. A high surface-to-volume ratio, which is characteristic of nano- and micro-particles, controls the interaction with pollutants and bacteria, conferring an increased efficiency compared to bulk materials [1,2].

Nanostructured metal oxides have a wide range of applications, including for catalysis and electronic and photonic devices [1,3,4]. They show exceptional potential for the photocatalytic breakdown of pollutants as they are considered safe, insoluble in water, and biologically inert [5–7]. Magnesium oxide (MgO), a wide band gap insulator, has been used primarily as a ceramic material in thermal engineering and heating elements and for refractory purposes. Fundamental and application studies have developed less conventional ways of exploiting its properties, which include catalysis, in toxic wastes remediation, and as an antibacterial agent. Micro- and nano-structured oxide powders have different properties from the bulk material form, and their reactivity capability is due to surface defects that include low coordination ions and/or vacancies [1,3]. The various defects

created in magnesium oxide's structure are considered intermediate energy levels inside the band gaps. In principle, a decrease in band gap energy suggests the possibility that photogenerated electrons from the conduction band of MgO are transferred to the defect centers, thus preventing their recombination with the h^+ species. This effect contributes, along with other properties that can be varied from the synthesis method (porosity, surface area, morphology, and size), to the high photocatalytic activity of magnesium oxide, as has been reported in the literature [8–12]. In addition, the ability of MgO nanoparticles to generate reactive oxygen species, such as $\cdot O_2^-$ and $\cdot OH$, confers them antibacterial properties [9,13,14], and their porous nature makes them suitable for waste remediation, allowing the adsorption of pollutants [15,16].

Several preparation methods for magnesium oxide have been developed with the aim of generating nanoscale particles with active surfaces, including dehydration of the $Mg(OH)_2$, thermal decomposition of various precursors [17], the sol–gel method [18,19], chemical vapor deposition [20], the hydrothermal method [21], and surfactant methods [22].

Thus, developing a simple procedure for preparing small-sized MgO powders under mild conditions has remained a challenging topic of investigation [1].

The sol–gel process is a bottom-up synthesis method in which the final product is formed by several irreversible reactions. The reaction rate depends on various factors such as pH, concentration, type of solvent, and temperature. Sol–gel-generated MgO powders have high surface areas and particular morphological and physical properties [23,24].

Hydrothermal precipitation is another promising method because the material resulting under mild reaction parameters can be nanostructured, with high crystallinity and various morphologies. Samples of MgO prepared using hydrothermal synthesis show emission peaks at 395 nm and 475 nm, and these are due to surface defects since nanoparticles exhibit a quantum confinement effect [25,26].

Of the many methods employed for the fabrication of MgO, microwave irradiation has recently gained interest over conventional methods due to its short duration, small investment, and its success in manipulating the morphology and architecture of nano- and micro-structures [27,28]. The effect of particle size, pH, and form of active MgO species obtained by microwave-assisted synthesis on the oxide's properties has been demonstrated by showing its bactericidal performance in an aqueous environment due to the superoxide formation [24,29].

A brief literature survey regarding the chemical methods of MgO preparation in solution is presented in Table 1. The hydrothermal and sol–gel methods are well-represented in the literature, with a variety of precursors and synthesis parameters. The microwave irradiation method is less common due to its novelty statism but is increasingly used due to its advantages, as described above.

Table 1. Literature survey of similar synthesis methods.

| Methods and Parameters | Precursors/Catalysts/Solvents | Thermal Treatment | Crystalline Phases and Morphologies | Ref. |
|-----------------------------------|---|-------------------|--|------|
| MW–360 W, 2 min, (on/off at 30 s) | $Mg(CH_3COO)_2 \times 4H_2O$ benzylamine | 550 °C for 5 h | MgO nanoparticles | [30] |
| MW–1 kW, 20 min (convection mode) | $Mg(CH_3COO)_2 \times 4H_2O$ <i>A. paniculata</i> extract | 400 °C for 2 h | MgO nanorods | [13] |
| MW–15 min | Magnesium nitrate, NaOH, H ₂ O | 400 °C for 4 h | MgO nanoparticles | [31] |
| MW–850 W, 15 min | Magnesium nitrate, urea, H ₂ O | 500 °C for 2 h | MgO nanosheets | [32] |
| HT–150 °C, 3 h | $MgCl_2 \times 6H_2O$, 1-Propanol, Urea (or NaOH), 2,4,6-trinitrophenol, H ₂ O | 600 °C for 3 h | MgO nanorods (urea) and nanoparticles (NaOH) | [16] |
| HT–180 °C, 24 h | magnesium nitrate, NaOH, and H ₂ O | 400 °C for 2 h | MgO nanoparticles | [33] |

Table 1. Cont.

| Methods and Parameters | Precursors/Catalysts/Solvents | Thermal Treatment | Crystalline Phases and Morphologies | Ref. |
|------------------------|--|-----------------------------------|--|------|
| HT-60 °C, 3–96 h | MgCl ₂ , Na ₂ CO ₃ , and H ₂ O | 200 °C for 2 h | MgO spheroidal and flake (or) rectangular particles | [34] |
| HT-120 °C for 12 h | Mg(NO ₃) ₂ × 6H ₂ O, CO(NH ₂) ₂ , sodium dodecyl sulfate, and H ₂ O | 400 °C for 5 h | MgO nanosheets | [35] |
| HT-180 °C for 10 h | Mg(NO ₃) ₂ × 6H ₂ O, H ₂ O, and ethanol | 500 °C for 3 h | MgO nanowires | [36] |
| HT-80–200 °C for 2 h | 50 nm MgO particles and H ₂ O | 300 °C for 1 h, 450 °C for 1 h | MgO plate-like shape | [37] |
| HT-200 °C for 24 h | Mg(NO ₃) ₂ × 6H ₂ O, urea, and H ₂ O | 500 °C for 5 h | MgO mesoporous | [38] |
| HT-150 °C for 24 h | Mg(NO ₃) ₂ × 6H ₂ O, NaOH, and H ₂ O | 400 °C for 4 h | MgO flower-like shape | [31] |
| HT-130 °C for 6 h | I. (NH ₄) ₂ CO ₃ , Mg(NO ₃) ₂ , and H ₂ O II. nesquehonite, (NH ₄) ₂ CO ₃ , and H ₂ O | 500 °C for 6 h | MgO random flakes, house-of-cards, spherical structures | [39] |
| HT-180 °C for 5 h | Mg(CH ₃ COO) ₂ × 4H ₂ O, urea, and H ₂ O (pH 8) Mg(CH ₃ COO) ₂ × 4H ₂ O, urea, acetic acid, and H ₂ O (pH 5–6) Mg(CH ₃ COO) ₂ × 4H ₂ O, urea, ammonia, and H ₂ O (pH 9–10) | 500 °C for 5 h | MgO mesoporous ball-like rhombohedrons (pH 5), smaller micro-rods (pH 9), and micro-rod-like (higher pH) | [40] |
| SG | 0.1 mM Mg(NO ₃) ₂ × 6H ₂ O, 0.1 M NaOH, and 100 mL H ₂ O | 400 °C for 4 h | MgO + Mg(OH) ₂ | [31] |
| SG | Mg(NO ₃) ₂ × 6H ₂ O and NaOH 1:2 M ratio of Mg ²⁺ to OH ⁻ | 400 °C for 5 h | MgO spherical nanoparticles | [14] |
| SG | 8.96 wt. % Mg MeO in MeOH sol., PhMe, and MeOH hydrolysis ratio = 2 M vol. ratio PhMe: MeOH = 0.94 | 400 °C (vacuum) | MgO | [41] |
| modified thermal/SG | Mg(C ₂ H ₃ O ₂) ₂ /Mg(NO ₃) ₂ , NaOH/NH ₄ OH, sodium dodecyl sulfate, and H ₂ O | 400–700 °C for 2 h | MgO + MgSO ₄ (traces), porous, agglomerated, and uniform semi-spherical flaky shape MgO | [15] |
| SG | Mg(CH ₃ COO) ₂ × 4H ₂ O C ₂ H ₂ O ₄ × 2H ₂ O/C ₄ H ₆ O ₆ , C ₂ H ₅ OH, and H ₂ O (pH 5) | 400 °C 500 °C | MgO + MgC ₂ O ₄ MgO nanocrystals | [42] |
| SG | MgCl ₂ and C ₆ H ₈ O ₇ × H ₂ O Mg ²⁺ : C ₆ H ₈ O ₇ = 1:3 T = 60 °C | 500 °C for 2 h | MgO spherical particles | [43] |
| SG | Mg(NO ₃) ₂ × 2H ₂ O, Pluronic P123, NH ₄ OH (28%), and H ₂ O pH 10 and T = 60 °C | 600 °C for 2 h | MgO nanoparticles | [44] |
| SG | Mg(NO ₃) ₂ × 6H ₂ O, NaOH, and H ₂ O 30 min ultrasonic stirring | 400 °C for 3 h | MgO nanosphere | [32] |
| SG | Mg(NO ₃) ₂ × 6H ₂ O, NaOH, NH ₄ OH, and H ₂ O molar ratio Mg ²⁺ :OH ⁻ = 1:2 | 500 °C for 4 h | MgO nanoparticles | [24] |
| SG | Mg(NO ₃) ₂ × 6H ₂ O, NaOH, and H ₂ O pH 12 | 500 and 800 °C for 4 h | MgO nanoparticles | [45] |
| SG | Mg(OCH ₃) ₂ and H ₂ O 40 h at RT | 500 and 600 °C for 4 h | MgO | [46] |
| SG | Mg(OCH ₃) ₂ , C ₂ H ₅ OH, HCl, NH ₄ OH, and H ₂ O pH 9 and 40 h reflux | 400, 600 and 800 °C for 2 h | MgO particles | [47] |

In our study, for comparison, MgO was obtained by three methods: sol–gel, hydrothermal, in which Mg(NO₃)₂ × 6H₂O was the precursor treated with a precipitating agent, and microwave-assisted sol–gel, which involved Mg(CH₃COO)₂ × 4H₂O precipitation with ammonia. The structure and morphology of the oxide powders obtained by these synthesis methods were characterized. Their photocatalytic activities were evaluated by monitoring

the photodegradation of methyl orange dye as a model pollutant under UV light irradiation, and the band gaps were determined. The results were discussed comparatively.

2. Results and Discussion

MgO powders prepared by the sol-gel, hydrothermal, and microwave-assisted sol-gel methods were investigated. An attempt was made to compare their structural and morphological properties and correlate them with their photocatalytic activities.

2.1. Phase Composition Investigation

Figure 1 presents the XRD diffractograms of the three thermally treated samples at 450 °C, depending on the preparation method. The main crystalline phase in all three samples was periclase, MgO, according to ICDD file no. 45-0946. The sample prepared by the microwave method contained single-phase periclase. The samples prepared by the sol-gel and hydrothermal methods also contained phases of brucite (ICDD file no. 44-1482) and hydromagnesite (ICDD file no. 25-0513) in addition to the main periclase phase. The quantitative ratios between the three phases, determined by the RIR (reference intensity ratio) method, are listed in Table 2.

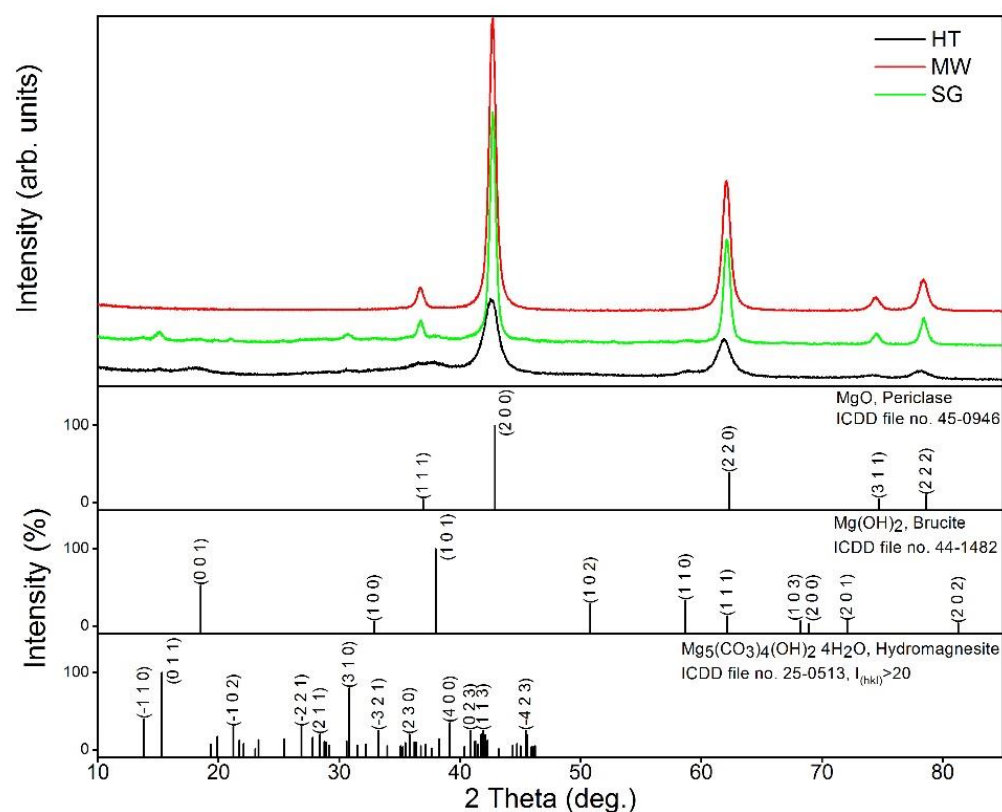


Figure 1. XRD patterns of the samples prepared by the microwave, sol-gel, and hydrothermal methods thermally treated at 450 °C.

Table 2 contains information regarding the crystalline phases present in the samples, the lattice parameters (only for periclase), the crystallite sizes (D_{XRD}) calculated by the Scherrer method, and the quantitative ratios.

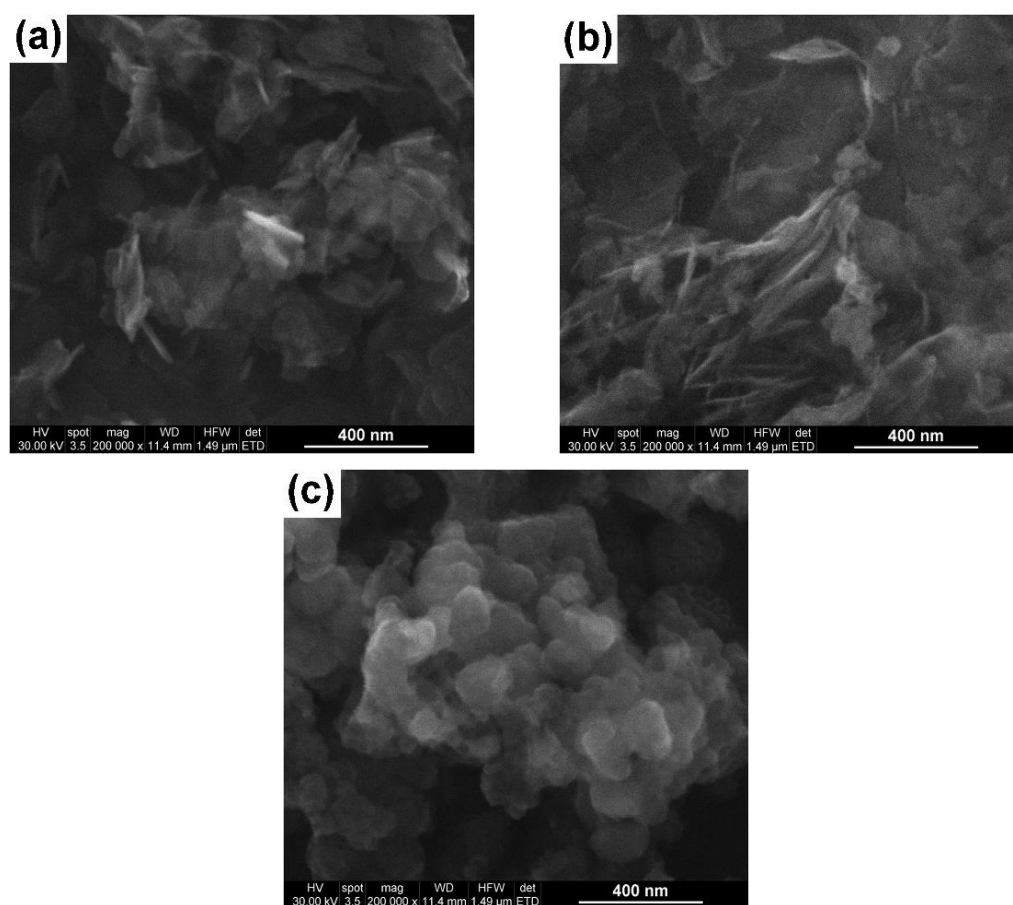
The sample prepared by the sol-gel method had the largest crystallite sizes for the periclase phase while the smallest crystallite sizes for the periclase phase were found in the sample prepared by the hydrothermal method. Regarding the lattice parameters of the unit cells of the periclase crystals, the smallest values were determined for the sample prepared by the sol-gel method while the largest values were found in the sample prepared by the hydrothermal method.

Table 2. Phase compositions, lattice parameters, crystallite sizes, and quantitative ratios.

| Sample | Phase(s) | Lattice Parameters (Å) | Crystallite Size, D_{XRD} (nm) | Quantitative Ratio (%) |
|--------|---|------------------------|----------------------------------|------------------------|
| MW | Periclase, MgO | 4.22569(5) | 10 | 100 |
| HT | Periclase, MgO | 4.23557(17) | 6 | 88.5 |
| | Brucite, Mg(OH) ₂ | - | - | 7.7 |
| | Hydromagnesite, Mg ₅ (CO ₃) ₄ (OH) ₂ × 4H ₂ O | - | - | 3.8 |
| SG | Periclase, MgO | 4.21986(11) | 15 | 87.7 |
| | Brucite, Mg(OH) ₂ | - | - | 3.3 |
| | Hydromagnesite, Mg ₅ (CO ₃) ₄ (OH) ₂ × 4H ₂ O | - | - | 9 |

2.2. Morphological, Structural, and Elemental Analyses

Figure 2 shows SEM images of the MgO particles prepared by the three above-mentioned methods. Both the hydrothermally synthesized and the sol-gel MgO powders consisted of non-uniform particles in terms of their sizes, with no clearly defined shapes (Figure 2a,b). Unlike them, the powdered sample synthesized using the microwave procedure exhibited well-defined, nearly spherical MgO particles, with sizes ranging between 80 and 120 nm (Figure 2c). To better observe the details regarding the morphological features and crystallinities of the particles prepared by the three mentioned methods, TEM, HRTEM, and SAED investigations were performed.

**Figure 2.** SEM images of the MgO particles: (a) MgO HT, (b) MgO SG, and (c) MgO MW.

The bright-field TEM images showed that there were significant morphological differences depending on the preparation route. The hydrothermally prepared sample consisted of unevenly sized thin MgO particles, most of which had a tabular and rod-like morphology (Figure 3a), with their crystallinities confirmed by the long-range ordered fringes revealed by the HRTEM image shown in Figure 3f. It is worth mentioning that the so-called “tabular particles” actually represented aggregates with an average size (d_{TEM}) of 106 ± 38 nm, as indicated in the histogram in Figure 3c. These aggregates were formed by a 2D self-assembly process of very small polyhedral crystallites with sizes well below 10 nm, as the enlarged image (Figure 3b) corresponding to the dashed red ellipse in Figure 3a reveals. A value for the average crystallite size in the HRTEM images could be only roughly estimated because of the tendency of the crystallites to overlap, which prevented a clear identification of their outlines. Nevertheless, the estimated values of the crystallite sizes ($D_{\text{TEM}} = 5 \pm 1$ nm) (Figure 3e) were close (within the error bar) to those determined from the XRD data, which indicated the smallest crystallite size ($D_{\text{XRD}} = 6$ nm) for this sample. On the other hand, the rod-like particles seemed to appear when, towards the end of the hydrothermal treatment, the spherical structures collapsed and recrystallized preferentially on the *c*-face of the crystallites [9]. As with the tabular particles, these rod-like structures of various values of length, *L*, and width, *l*, were also aggregates of small crystallites (the dashed cyan ellipses in Figure 3a). An average value of the aspect ratio (expressed as *L/l* and noted as *a.r.*) of 12 ± 5 was determined from the measurements carried out on ~40 rods from different areas of the TEM images (Figure 3d). A certain amount of amorphous phase was also present in this powder as the continuous and slightly diffuse aspect of the concentric rings in the related SAED image shows (Figure 3g).

The powdered sample prepared by the sol-gel method exhibited a duplex-type morphology (Figure 4a) where elongated or enlarged thin foils (denoted by A), structured as nanosized crystallites, coexisted with individual particles (denoted by B) of polyhedral shapes with well-defined edges and rounded corners. These particles appeared to be single crystals as they showed no structuring, as can be observed in the higher magnification TEM image in Figure 4b. For the individual particles, an average size (d_{TEM}) of 40 ± 9 nm was estimated (Figure 4c). In this case, the crystallites that built up the thin foils appeared to be slightly larger in size ($D_{\text{TEM}} = 13 \pm 2$ nm) (see Figure 4d) than those observed for the hydrothermal powder discussed above. The HRTEM image in Figure 4e and the SAED pattern in Figure 4f also reveal an increased crystallinity which showed small bright spots that formed the diffraction rings.

By microwave irradiation, the basic magnesium oxide particles, acting as nucleation sites, gradually formed the small and dispersed initial centers that aggregated, generating microspheres [27]. Indeed, the TEM image in Figure 5a shows that the single-phased MgO powder prepared by this technique consisted of nearly spherical aggregates with an average size (d_{TEM}) of 96 ± 14 nm (Figure 5b). A look inside these aggregates revealed their structuring in small, polyhedral crystallites (Figure 5c), somewhat similar to those observed in the sol-gel powder. An average crystallite size value of $D_{\text{TEM}} = 10 \pm 2$ nm, similar to that determined from the XRD data (Table 1), was found in this case (Figure 5d). Therefore, based on the TEM investigations, we concluded that the particles from the SEM image in Figure 2c were aggregates of crystallites strongly bound together. In addition, for this powder, the related HRTEM image showed a high crystallinity degree (Figure 5e). However, the more diffuse aspect of the diffraction rings in the corresponding SAED pattern, consisting of fewer bright spots than the sol-gel powder, indicated an intermediate crystallinity (somewhat lower than that of the sol-gel powder but higher than that determined for the hydrothermally processed MgO sample), which was in agreement with the values estimated for the average crystallite size (Figure 5f).

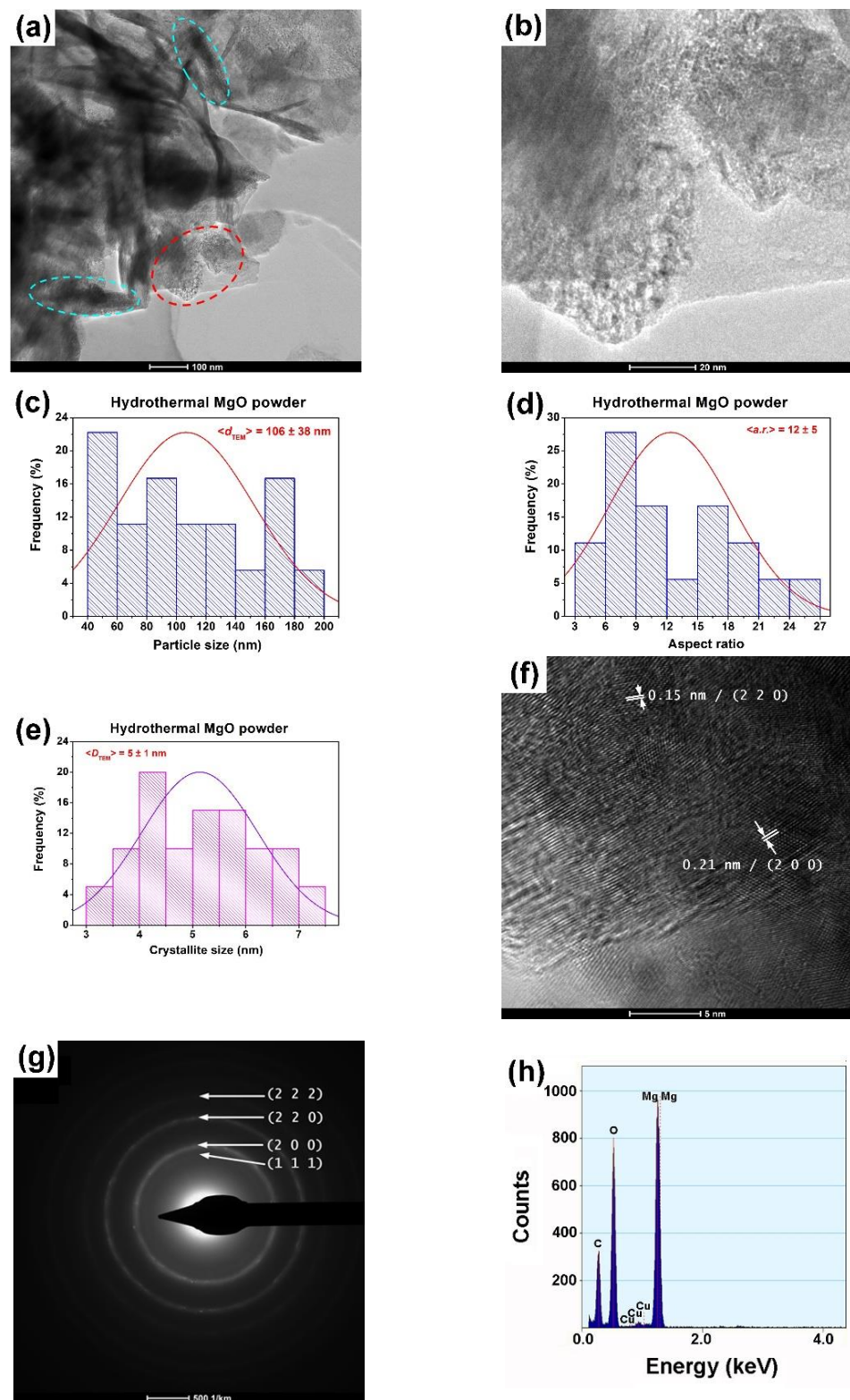


Figure 3. Low (a) and high (b) magnification TEM images (dashed red ellipse indicates the tabular particles and dashed cyan ellipses rod-like structures); size distribution of the tabular aggregates (c); aspect ratio (*a.r.*) distribution of the rod-like aggregates histogram (d); crystallite size distribution histogram (e); HRTEM image (f); SAED pattern (g); and EDX spectrum (h) of the hydrothermally prepared MgO powder.

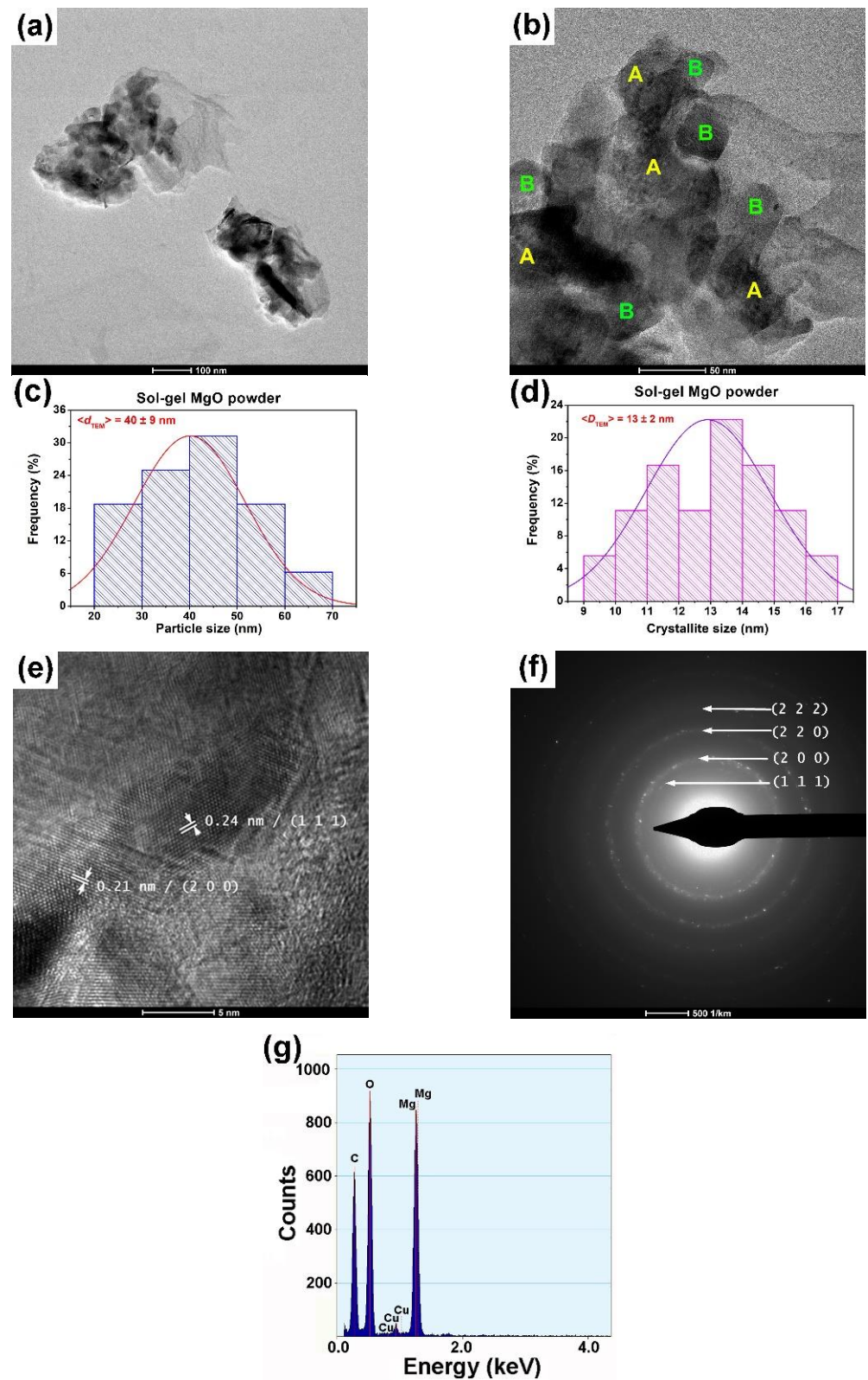


Figure 4. Low (a) and high (b) magnification TEM images (A corresponds to thin foils and B to individual particles of polyhedral shape); size distribution of the aggregates histogram (c); crystallite size distribution histogram (d); HRTEM image (e); SAED pattern (f); and EDX spectrum (g) of the sol-gel MgO powder.

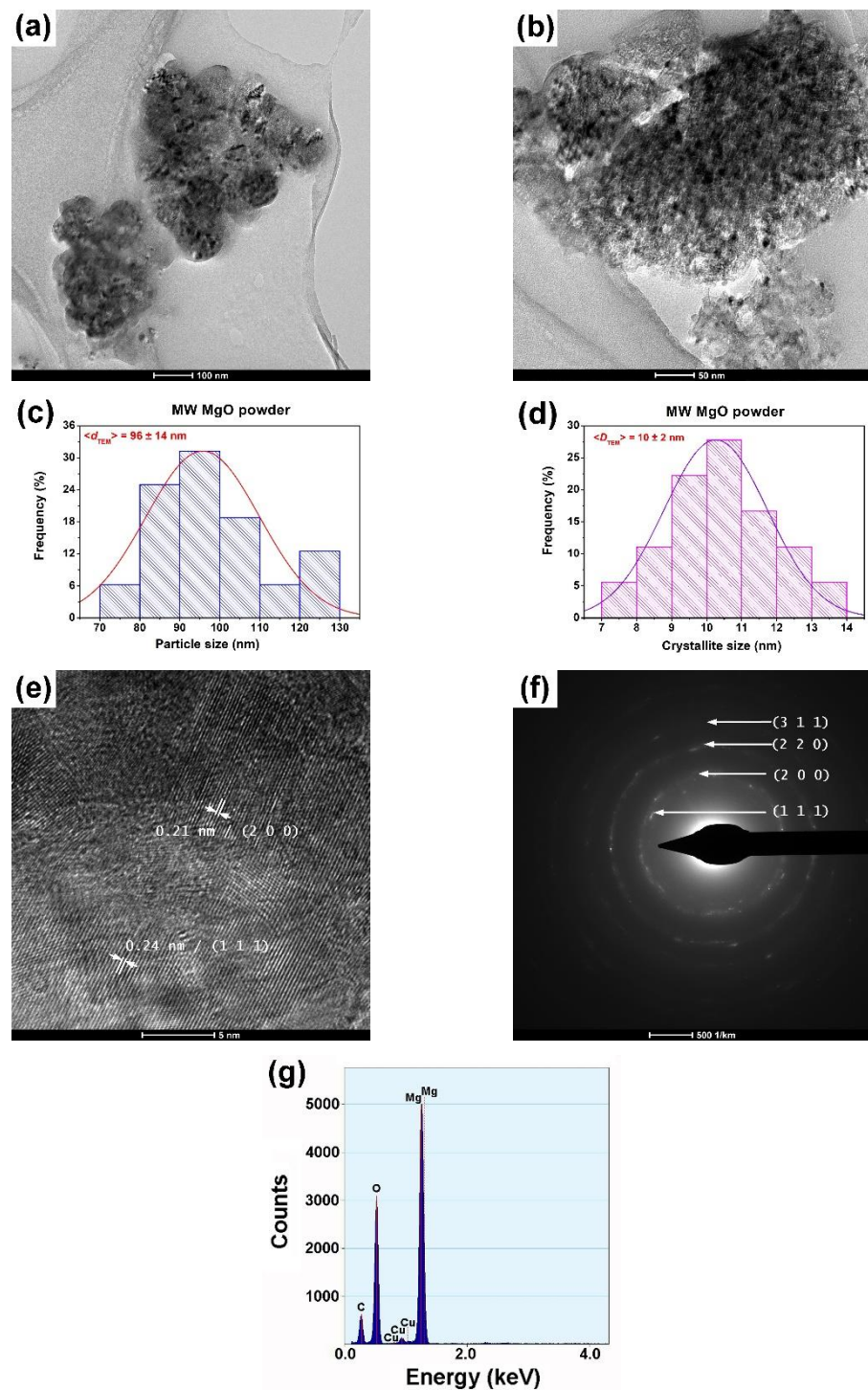


Figure 5. Low (a) and high (b) magnification TEM images; size distribution of the aggregates histogram (c); crystallite size distribution histogram (d); HRTEM image (e); SAED pattern; (f) and EDX spectrum (g) of the MW-assisted MgO powder.

During microwave-assisted combustion synthesis, gaseous products are released that create cavities in the initially formed oxide microspheres, generating defects that could act as catalytic sites [27]. Nano- and micro-scale materials (Figure 2) have large surface-to-volume ratios, resulting in the formation of voids on the surface as well as inside the agglomerated particles that cause absorption bands in the UV regions [25].

The EDX spectra of all three MgO powders under investigation showed the high chemical purity degrees of the samples (Figures 3h, 4g and 5g). Apart from the carbon

and copper atoms related to the TEM grids, only the presence of magnesium and oxygen species was detected, which suggested that no contamination occurred during the synthesis processes.

2.3. Textural Characterization

N_2 adsorption–desorption measurements were carried out to investigate the textural features of the MgO samples. All samples exhibited type IV isotherms with H3-type hysteresis loops, as shown in Figure 6. According to IUPAC classification [48], this type of isotherm is a characteristic of mesoporous materials while H3 hysteresis loops appear in materials with flexible pores with a slit or plate-like morphology or those that form particle agglomerates. Unlike the MgO MW sample, whose pore distribution range had a relatively narrow interval (0–20 nm), for the MgO HT and MgO SG samples, the pore sizes were greater than 20 nm and even exceeded the range of mesopores (2–50 nm). As can be seen in Table 3, MgO HT had the highest BET specific surface area, followed by MgO MW and MgO SG. Regarding the total volume of the pores, the order was different, namely, MgO HT > MgO SG > MgO MW. These findings confirmed the presence of porous structures in the prepared MgO samples.

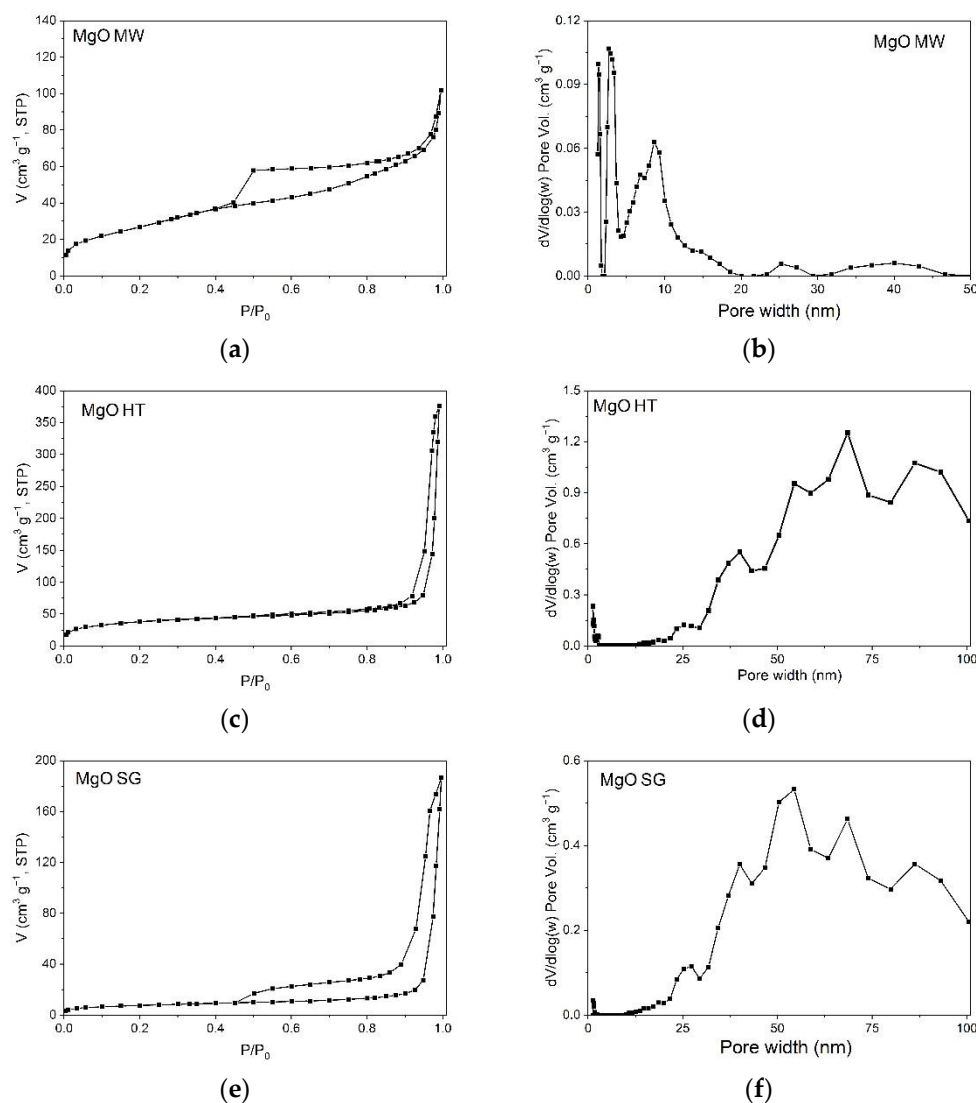


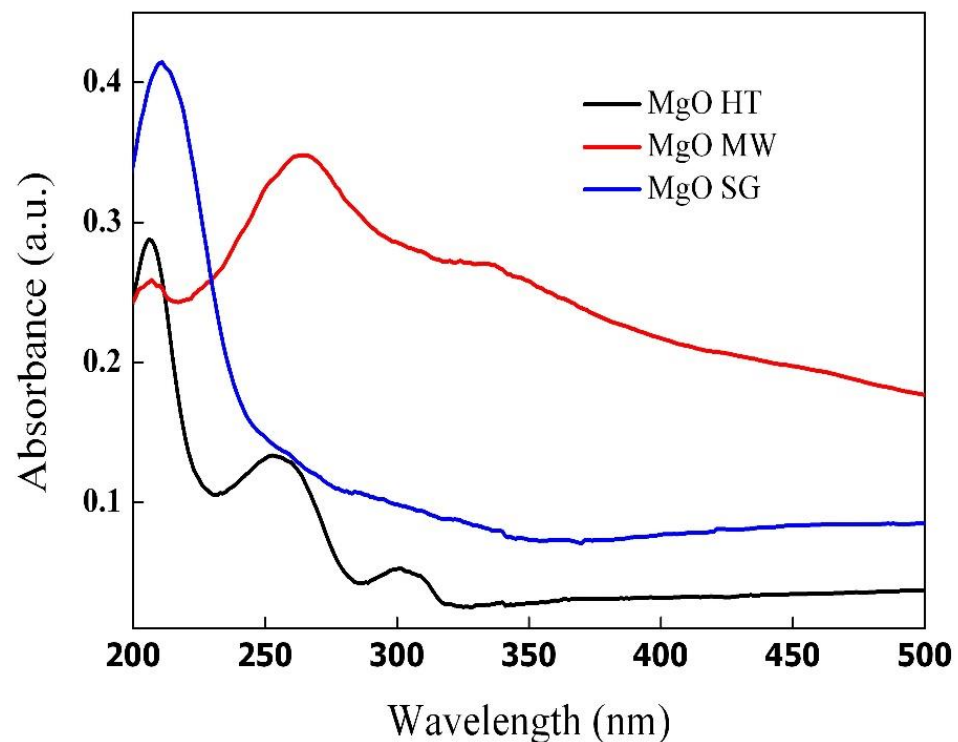
Figure 6. The nitrogen adsorption–desorption isotherms (a,c,e) and DFT pore size distributions (b,d,f) of the samples.

Table 3. The BET specific surface areas (S_{BET}), total pore volumes (V_{total}), and band gaps of the samples.

| Sample | S_{BET} (m^2g^{-1}) | V_{total} (cm^3g^{-1}) | Bandgap Energy (eV) |
|--------|---|--|---------------------|
| MgO MW | 101.1 | 0.157 | 3.94 |
| MgO HT | 132.1 | 0.562 | 4.48 |
| MgO SG | 26.3 | 0.289 | 5.32 |

2.4. UV–Vis Spectroscopy Analysis

The optical properties of the MgO samples synthesized by the three different methods were evaluated using UV–Vis spectroscopy, and the recorded spectra are shown in Figure 7. For all three samples, the absorption bands with the maximum values located at ~ 206 nm were assigned to the excitation of five coordinated oxygen anions from the periclase structure [49]. Additional absorption bands located at higher wavelengths could be assigned to various F-type defects generated during synthesis. The most intense absorption bands were noticed in the case of the magnesium oxide prepared by the microwave method. Thus, the peak located at ~ 255 nm suggested the presence of F^+ and F centers while the peaks recorded at wavelengths around 300 nm indicated the formation of some F_2^{2+} centers [49]. The same absorption bands were also observed for the MgO sample obtained by the hydrothermal method, indicating the formation of several structural defects. It has been previously reported [50] that during hydrothermal treatment, the generation of water molecules between neighboring hydroxyl ions and their losses cause the occurrence of defects in the MgO's structure. Furthermore, the formation of inter-crystallite channels and cracks and their contributions to higher specific surface areas than in the case of the sol–gel method (as was evident in the present study, see Table 3) was discussed [50].

**Figure 7.** UV–Vis absorption spectra of the MgO powders prepared by the three different methods.

The band gap energy for each sample was estimated by Tauc plots of the Kubelka–Munk function for direct transitions. The obtained results shown in Table 3 evidenced the effects of the synthesis methods on the bandgap energies of the MgO. Although magnesium oxide is a wide band-gap material (7.8 eV) [51], the synthesis methods proposed in the present work

lowered the band gaps due to the formation of different defects that acted as intermediate levels available for the transfer of excited electrons [49]. The values of the obtained band gaps are shown in Table 3. Thus, the lowest value was obtained for magnesium oxide prepared by the microwave method (3.94 eV), indicating that this preparation method is the most suitable for obtaining magnesium oxide with improved photocatalytic properties.

2.5. Photoluminescence (PL) Studies

The photoluminescence (PL) spectra recorded for the samples prepared by the three different methods are shown in Figure 8. For all the samples, the PL results showed broad emission bands in the violet and blue regions of the visible spectrum (410–490 nm) and a more intense and sharper peak in the green region (580 nm). These were mainly related to the presence of several defects in the MgO structures, depending on the synthesis method. Thus, the first emission peak located at 416 nm was associated with F centers resulting from the removal of neutral O atoms in the magnesium oxide structure while the peak that appeared at 440 nm could be attributed to the dimmers of the F center, such as F_2^{2+} [52,53]. The green emissions recorded for all the samples were mainly due to oxygen deficiencies in the structures of the synthesized magnesium oxides, as has been suggested in other studies [54,55].

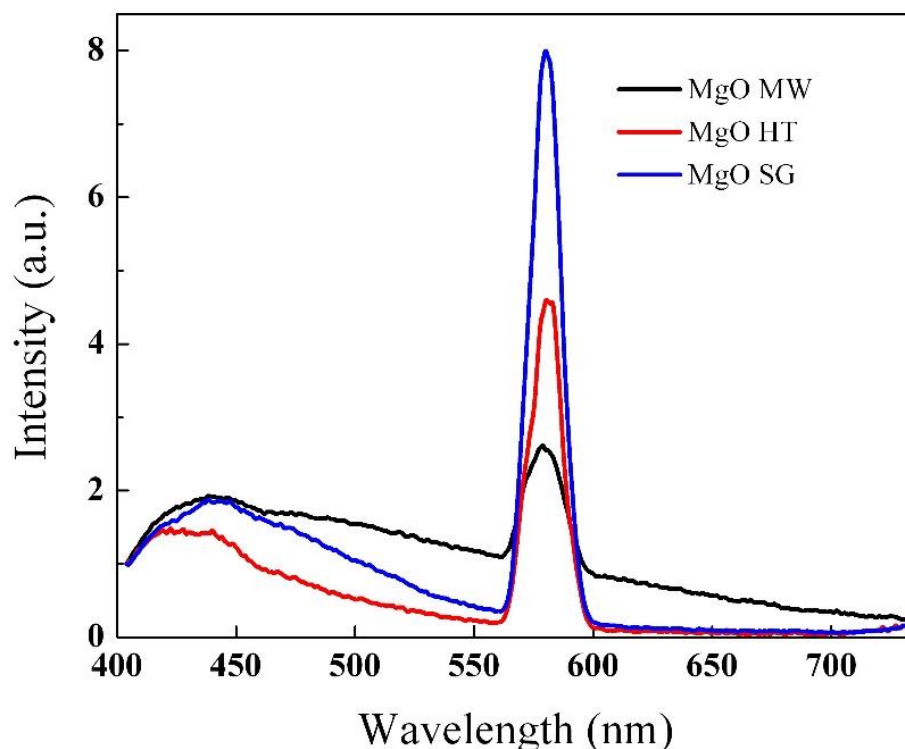


Figure 8. PL spectra of the MgO powders synthesized by the sol-gel (SG), microwave-assisted sol-gel (MW), and hydrothermal (HT) methods ($\lambda_{exc} = 385$ nm).

2.6. Photocatalytic Activity

The photocatalytic activities of magnesium oxide samples were investigated by carrying out the degradation of methyl orange (MO) dyes. The variations in MO degradation efficiencies over time in the presence of the MgO photocatalysts are shown in Figure 9. The highest photocatalytic activity was found for the MgO prepared by the microwave method due to the obtained properties, which were beneficial for photocatalytic applications. The large specific surface area, the low band gap energy, the presence of defects that contributed to delaying the recombination of the photogenerated charges, and the spherical morphology obtained by the microwave method were properties that had beneficial effects on its photocatalytic efficiency.

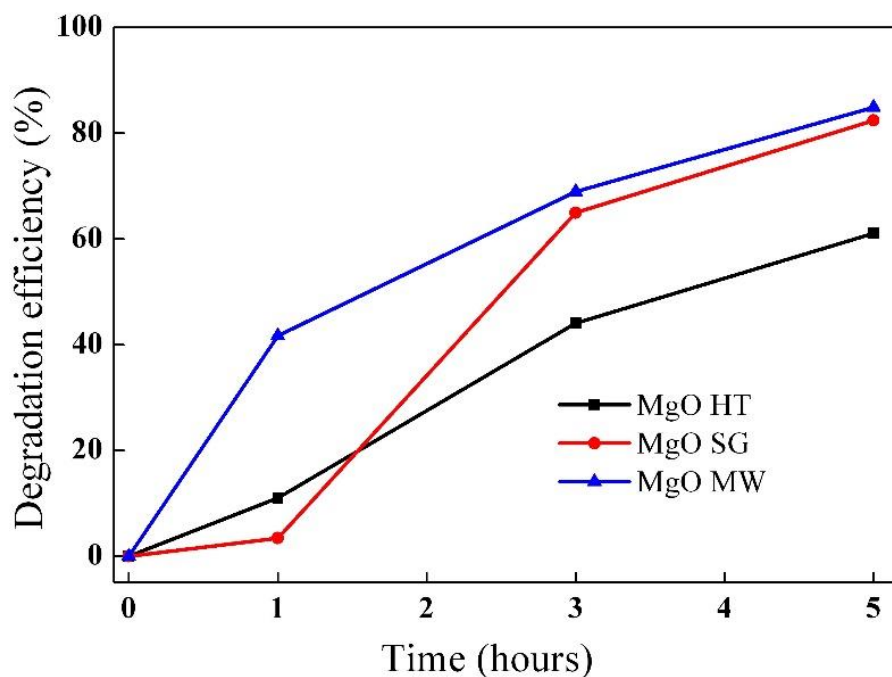


Figure 9. Photocatalytic performances of the MgO samples prepared by the three different methods ($\lambda_{\text{irrad.}} = 254 \text{ nm}$, $1 \times 10^{-5} \text{ M MO}$, and 5 mg of photocatalyst).

In the case of the other two samples obtained by the sol-gel and hydrothermal methods, although the efficiencies of methyl orange degradations were slightly lower, the photocatalytic results were comparable to those reported in the literature. A comparative analysis of these results is summarized in Table 4.

Table 4. A comparison of the photocatalytic results under UV light irradiation of MgO samples synthesized by different methods.

| Method | Phase | Band Gap (eV) | Degradation Efficiency (%) | Ref. |
|--|---|---------------|---|--------------|
| Thermal decomposition of $\text{Mg}(\text{OH})_2$ by the wet chemical method | Polycrystalline MgO with a cubic structure | 5.54 | 50% of methyl orange (10 mg/L) | [56] |
| Green synthesis | Cubic MgO structure | 4.17 | 81% of methylene blue (20 ppm) | [57] |
| Reflux condensation approach | Cubic MgO structure | 5.63 | 92% of methyl orange 95% of methylene blue | [1] |
| | | 5.67 | 96% of methyl orange 99% of methylene blue | |
| Combustion method | Polycrystalline cubic structure of MgO nanoparticles | - | 75% of methylene blue | [4] |
| Sol-gel method | Periclase, MgO brucite, $\text{Mg}(\text{OH})_2$ hydromagnesite, and $\text{Mg}_5(\text{CO}_3)_4(\text{OH})_2 \times 4\text{H}_2\text{O}$ | 5.32 | 82% of methyl orange ($1 \times 10^{-5} \text{ M}$) | |
| Hydrothermal method | Periclase, MgO brucite, $\text{Mg}(\text{OH})_2$ hydromagnesite, and $\text{Mg}_5(\text{CO}_3)_4(\text{OH})_2 \times 4\text{H}_2\text{O}$ | 4.48 | 61% of methyl orange ($1 \times 10^{-5} \text{ M}$) | Present work |
| Microwave-assisted sol-gel method | Periclase, MgO | 3.94 | 85% of methyl orange ($1 \times 10^{-5} \text{ M}$) | |

2.7. Identification of Reactive Species

To understand the action pathway of each MgO sample, photocatalytic experiments were carried out in the presence of $\cdot\text{O}_2^-$, $\cdot\text{OH}$, and e^- and h^+ scavengers. The results

obtained are shown in Figure 10. A higher degradation efficiency was obtained in the case of adding the e^- and h^+ scavengers. This behavior could be explained by the delay in the recombination of the e^-/h^+ pairs, which ensured a larger number of photo-generated species available for the degradation of the methyl orange. A slight increase in the photocatalytic efficiency was also obtained by adding $\cdot OH$ and $\cdot O_2^-$ scavengers, which suggested an equal contribution of these reactive species to the degradation of the methyl orange. Therefore, when the superoxide anions were captured from the reaction medium, hydroxyl radicals ($\cdot OH$), which are known as the most reactive oxygen species [58], became directly responsible for the degradation of the methyl orange molecules.

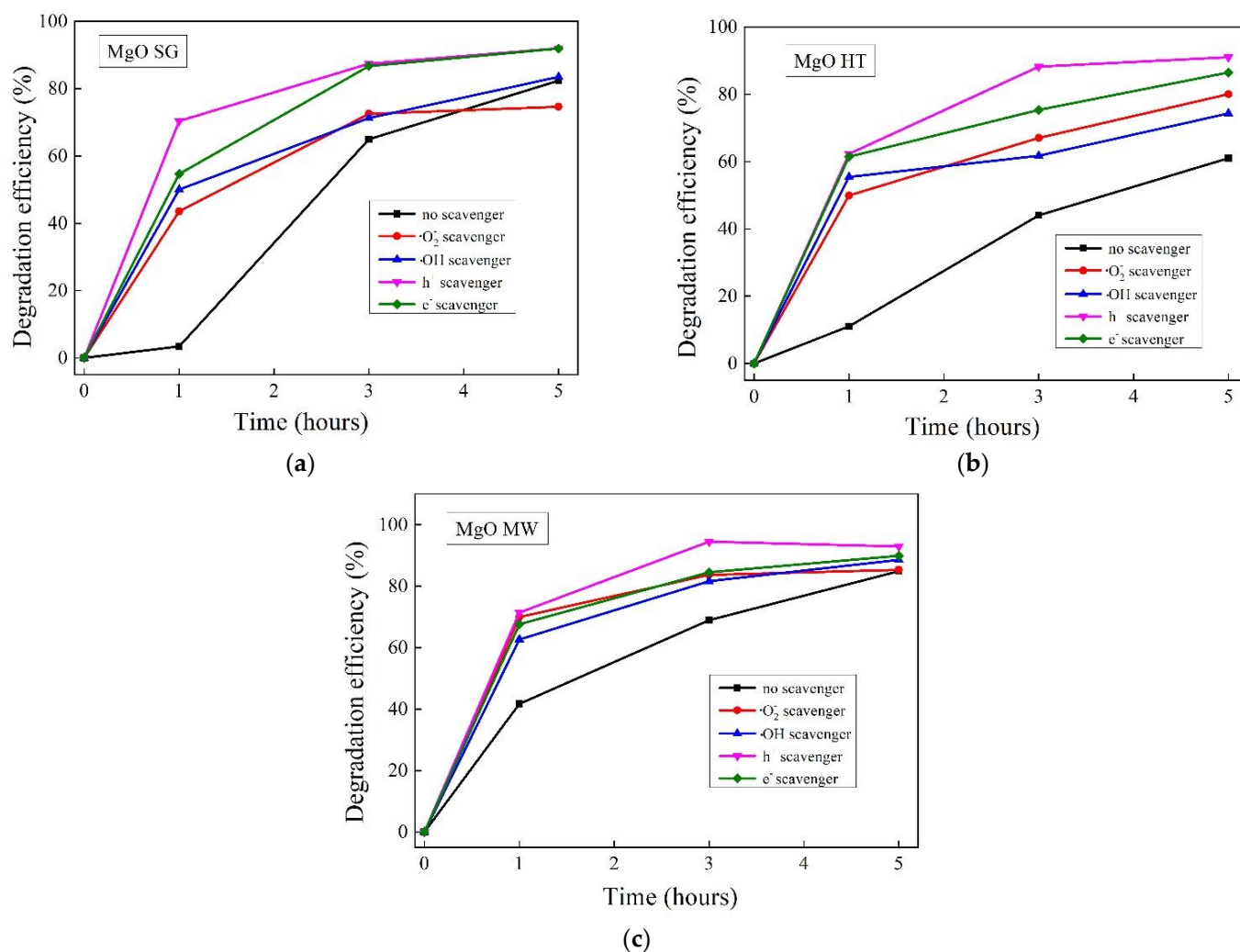


Figure 10. The effect of scavengers on the photocatalytic degradation of methyl orange by the MgO samples under UV light irradiation: (a) the sol-gel sample; (b) the hydrothermally prepared sample; and (c) the microwave-assisted sol-gel sample.

Based on these results, it could be concluded that all the investigated active species had important contributions to the photocatalytic degradation of the methyl orange. Thus, by quenching a reactive species, its resultant lack was compensated by all the others in the system. A schematic representation of the possible degradation mechanism of the methyl orange by the MgO powders and the relevant reactive species can be found in Figure 11.

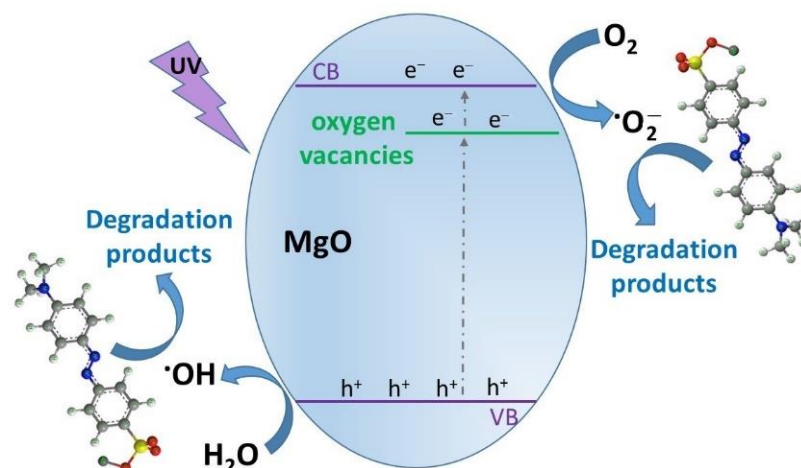


Figure 11. Schematic representation of the possible degradation mechanism of the methyl orange by the MgO samples.

3. Conclusions

The present study aimed to correlate the structural and morphological properties of MgO powders generated by different synthesis methods with their photocatalytic activities. All the samples had porous, nanoscale, and microscale structures. The particles obtained by the sol–gel method had the lowest specific surface areas and the highest optical band gaps. The powders prepared by the microwave method had higher specific surface areas, narrow nanopore distributions, and the lowest band gaps. Additional UV-Vis absorption bands in the case of the MgO powders prepared by the microwave and hydrothermal methods indicated that defects were generated during the synthesis.

The best photocatalytic activity (~85% degradation efficiency) was obtained after 5 h of irradiation for the MgO synthesized by the microwave-assisted sol–gel method, for which the lowest band gap energy (3.94 eV) was obtained and spherical morphology. The microwave method induced the formation of several structural defects that prevented e^-/h^+ recombination. Thus, the photocatalytic process was improved by providing a high number of photogenerated charges responsible for the degradation of the MO.

4. Materials and Methods

4.1. Powder Preparation

The MgO powders were obtained by the sol–gel method using $Mg(NO_3)_2 \times 6H_2O$ as a precursor in an ethanolic solution, H_2O as a hydrolyzing agent, and NH_4OH as the catalyst, according to the method presented in reference [59].

The hydrothermal synthesis started with the $Mg(NO_3)_2 \times 6H_2O$. The precipitating agent, NaOH, was dissolved in equal volume mixtures of water–ethanol, with the ratio of precursor/NaOH being 2/5, which was added to magnesium salt. The reaction system was kept under stirring until a white precipitate appeared, and then it was transferred to a hydrothermal cell heated at 130 °C, where it was kept for 14 h. After cooling at room temperature, the powder was separated by filtration, washed with distilled water, and dried, and then it thermally treated as mentioned in reference [59].

The microwave-assisted sol–gel method used $Mg(CH_3COO)_2 \times 4H_2O$ in a 0.3 M aqueous solution and ammonia as a catalyst. The mixture was kept under microwaves for 10 min (2.45 GHz and 1 kW). The precipitated powder was treated as mentioned above, and then it was thermally treated as follows: 450 °C, 1 h plateau, and 1 °C/min.

4.2. Powders Characterization

The X-ray diffraction (XRD) patterns were recorded using a Rigaku Ultima IV X-ray diffractometer (Tokyo, Japan). The equipment was set in a parallel beam geometry with

cross beam optics (CBO) and operated at 40 kV and 30 mA using CuK α radiation. The data were collected over the 2 θ range at 10–85° at a scanning rate of 2 °/min. Rigaku's PDXL v1.8 software, connected to the ICDD PDF-2 database, was used for phase identification.

SEM, TEM, and HRTEM coupled with SAED and EDX (energy dispersive X-ray spectroscopy) investigations were performed using a high-resolution FEI QUANTA INSPECT F scanning electron microscope (Thermo Fisher Scientific, Waltham, MA, USA) with a field emission gun and a TITAN THEMIS ultra-high resolution electron microscope (Thermo Fisher Scientific, Waltham, MA, USA). For the acquisition of the EDX spectra, the transmission electron microscope was operated in STEM (scanning transmission electron microscopy) mode at 300 kV.

The average particle sizes of the BST powder were estimated from the particle size distributions, which were determined using OriginPro 8.5 software (OriginLab, Northampton, MA, USA) by taking into account size measurements for ~30 particles, which were performed by means of the software of the electron microscope (Digital Micrograph 1.8.0) (Gatan, Sarasota, FL, USA).

The nitrogen physisorption isotherms were measured at –196 °C using an ASAP 2020 instrument from Micromeritics (Norcross, GA, USA). Before taking the measurements, the samples were outgassed under a vacuum at 250 °C for 4 h. The specific surface areas of the materials were assessed by the Brunauer–Emmet–Teller (BET) method, while the total pore volumes were calculated from the amounts adsorbed at relative pressures of 0.99. Pore size distributions were estimated using the density functional theory (DFT) method provided by the software of the ASAP 2020 instrument.

The morphologies of the MgO nanopowders were observed by field emission scanning electron microscopy (SEM) using a Quanta 3D FEG Dual Beam (Eindhoven, The Netherlands).

The UV–Visible absorption spectra of the MgO samples were recorded using a JASCO V570 spectrophotometer (Tokyo, Japan).

An FLSP 920 spectrofluorometer (Edinburgh Instruments, Livingston, UK) was used for recording the photoluminescence spectra (PL) of the magnesium oxide samples. The excitations at wavelengths of 385 nm were achieved with the help of an Xe lamp. The PL spectra were recorded at room temperature between 400 and 750 nm.

The photocatalytic reactions were carried out in a closed room at 30 °C. A total of 5 mg of MgO photocatalyst was added to a 10 mL solution of methyl orange dye (1×10^{-5} M). The mixture was firstly stirred in the dark for 30 min to allow the dye molecules to adsorb on the magnesium oxide surface. Then, irradiation at $\lambda = 254$ nm using a UV-VL-215c lamp was started, and it continued for 5 h. After 1, 3, and 5 h of irradiation, the photocatalyst was then separated from the suspension using a Millipore syringe filter (0.45 μ m). The filtered solution was spectrophotometrically analyzed using the same JASCO V570 spectrophotometer to evaluate the dye degradation progress. The degradation efficiency was calculated as $D_{\text{eff}} = (A_0 - A_t)/A_0 \times 100$, where A_0 is the absorbance of the initial MO solution and A_t is the absorbance at a particular interval of time.

To investigate the main active species responsible for the MO degradation, scavenger experiments were undertaken. In this regard, p-benzoquinone (p-BQ) was used as a quencher for the superoxide radicals ($\cdot\text{O}_2^-$), ethanol was used for the hydroxyl radicals ($\cdot\text{OH}$), silver nitrate was used for the electrons, and potassium iodide was used for the holes. The scavenger's concentrations were 0.1 mM, and the reaction conditions were the same as in the photocatalytic experiments.

Author Contributions: Conceptualization, L.T. and L.P.; methodology, L.P.; investigation, L.T., L.P., G.P., S.P., D.C.C., A.B., R.-D.T., V.-A.S. and B.S.V.; resources, A.-C.I. and L.P.; writing—original draft preparation, L.T., L.P., G.P., S.P., D.C.C., A.B. and A.-C.I.; writing—review and editing, L.T., L.P., G.P., S.P. and A.-C.I.; visualization, L.P. and S.P.; project administration, L.P. All authors have read and agreed to the published version of the manuscript.

Funding: This research was funded by the Romanian Ministry of Research and Innovation, grant number PCCDI-UEFISCDI, project number PN-III-P1-1.2-PCCDI-2017-0476/51PCCDI/2018.

Institutional Review Board Statement: Not applicable.

Informed Consent Statement: Not applicable.

Data Availability Statement: All data are available upon reasonable request from the authors.

Acknowledgments: This work was supported by the research program “Materials Science and Advanced Methods for Characterization” of the Institute of Physical Chemistry “Ilie Murgulescu” and financed by the Romanian Academy.

Conflicts of Interest: The authors declare no conflict of interest.

References

1. Mageshwari, K.; Mali, S.S.; Sathyamoorthy, R.; Patil, P.S. Template-Free Synthesis of MgO Nanoparticles for Effective Photocatalytic Applications. *Powder Technol.* **2013**, *249*, 456–462. [[CrossRef](#)]
2. Tahir, M.; Sohaib, M.; Sagir, M.; Rafique, M. Role of Nanotechnology in Photocatalysis. *Encycl. Smart Mater.* **2022**, *2*, 578–589. [[CrossRef](#)]
3. Cui, H.; Wu, X.; Chen, Y.; Boughton, R.I. Synthesis and Characterization of Mesoporous MgO by Template-Free Hydrothermal Method. *Mater. Res. Bull.* **2014**, *50*, 307–311. [[CrossRef](#)]
4. Balakrishnan, G.; Velavan, R.; Mujasam Batoo, K.; Raslan, E.H. Microstructure, Optical and Photocatalytic Properties of MgO Nanoparticles. *Results Phys.* **2020**, *16*, 103013. [[CrossRef](#)]
5. Haounati, R.; Ighnih, H.; Malekshah, R.E.; Alahiane, S.; Alakhras, F.; Alabbad, E.; Alghamdi, H.; Ouachtak, H.; Addi, A.A.; Jada, A. Exploring ZnO/Montmorillonite Photocatalysts for the Removal of Hazardous RhB Dye: A Combined Study Using Molecular Dynamics Simulations and Experiments. *Mater. Today Commun.* **2023**, *35*, 105915. [[CrossRef](#)]
6. Zhu, X.; Wang, J.; Yang, D.; Liu, J.; He, L.; Tang, M.; Feng, W.; Wu, X. Fabrication, Characterization and High Photocatalytic Activity of Ag–ZnO Heterojunctions under UV-Visible Light. *RSC Adv.* **2021**, *11*, 27257–27266. [[CrossRef](#)] [[PubMed](#)]
7. Haounati, R.; Ighnih, H.; Ouachtak, H.; Malekshah, R.E.; Hafid, N.; Jada, A.; Ait Addi, A. Z-Scheme g-C₃N₄/Fe₃O₄/Ag₃PO₄@Sep Magnetic Nanocomposites as Heterojunction Photocatalysts for Green Malachite Degradation and Dynamic Molecular Studies. *Colloids Surf. Physicochem. Eng. Asp.* **2023**, *671*, 131509. [[CrossRef](#)]
8. Aziz, B.K.; Karim, M.A.H. Efficient Catalytic Photodegradation of Methylene Blue from Medical Lab Wastewater Using MgO Nanoparticles Synthesized by Direct Precipitation Method. *React. Kinet. Mech. Catal.* **2019**, *128*, 1127–1139. [[CrossRef](#)]
9. Karthik, K.; Dhanuskodi, S.; Gobinath, C.; Prabukumar, S.; Sivaramakrishnan, S. Fabrication of MgO Nanostructures and Its Efficient Photocatalytic, Antibacterial and Anticancer Performance. *J. Photochem. Photobiol. B* **2019**, *190*, 8–20. [[CrossRef](#)]
10. Dobrucka, R. Synthesis of MgO Nanoparticles Using Artemisia Abrotanum Herba Extract and Their Antioxidant and Photocatalytic Properties. *Iran. J. Sci. Technol. Trans. Sci.* **2018**, *42*, 547–555. [[CrossRef](#)]
11. Gingas, D.; Mindru, I.; Culita, D.C.; Predoana, L.; Petcu, G.; Ciobanu, E.M.; Preda, S.; Pandele-Cusu, J.; Petrescu, S. MgO Obtained by Chemical and Green Synthesis Methods and Applied in Photocatalytic Degradation of Methyl Orange. *Rev. Roum. Chim.* **2021**, *66*, 463–473.
12. Matsukevich, I.; Atkinson, I.; Besarab, S.; Petcu, G.; Petrescu, S.; Parvulescu, V.; Fruth, V. Composite Materials Based on MgO and Metallic Nanoparticles for Catalytic Applications (in RO: Materiale Compozite Pe Bază de MgO Și Nanoparticule Metalice Pentru Aplicații Catalitice). *Rev. Romana Mater. (Rom. J. Mater.)* **2019**, *49*, 483–490.
13. Karthik, K.; Dhanuskodi, S.; Prabu Kumar, S.; Gobinath, C.; Sivaramakrishnan, S. Microwave Assisted Green Synthesis of MgO Nanorods and Their Antibacterial and Anti-Breast Cancer Activities. *Mater. Lett.* **2017**, *206*, 217–220. [[CrossRef](#)]
14. Bindhu, M.R.; Umadevi, M.; Kavimicheal, M.; Arasu, M.V.; Abdullah Al-Dhabi, N. Structural, Morphological and Optical Properties of MgO Nanoparticles for Antibacterial Applications. *Mater. Lett.* **2016**, *166*, 19–22. [[CrossRef](#)]
15. Mashayekh-Salehi, A.; Moussavi, G.; Yaghmaeian, K. Preparation, Characterization and Catalytic Activity of a Novel Mesoporous Nanocrystalline MgO Nanoparticle for Ozonation of Acetaminophen as an Emerging Water Contaminant. *Chem. Eng. J.* **2017**, *310*, 157–169. [[CrossRef](#)]
16. Ali, S.; Farrukh, M.A.; Khaleeq-ur-Rahman, M. Photodegradation of 2,4,6-Trinitrophenol Catalyzed by Zn/MgO Nanoparticles Prepared in Aqueous-Organic Medium. *Korean J. Chem. Eng.* **2013**, *30*, 2100–2107. [[CrossRef](#)]
17. Mohandes, F.; Davar, F.; Salavati-Niasari, M. Magnesium Oxide Nanocrystals via Thermal Decomposition of Magnesium Oxalate. *J. Phys. Chem. Solids* **2010**, *71*, 1623–1628. [[CrossRef](#)]
18. Anchana, M.; Komathi, E.; Oviya, S.; Sabari, V. Synthesis and Characterization Studies of Pure MgO by Sol-Gel Method. *Int. J. Adv. Res. Sci. Commun. Technol.* **2021**, *12*, 22–26. [[CrossRef](#)]
19. Wahab, R.; Ansari, S.G.; Dar, M.; Kim, Y.S.; Shin, H.-S. Synthesis of Magnesium Oxide Nanoparticles by Sol-Gel Process. *Mater. Sci. Forum* **2007**, *558*, 983–986.
20. Hao, Y.; Meng, G.; Ye, C.; Zhang, X.; Zhang, L. Kinetics-Driven Growth of Orthogonally Branched Single-Crystalline Magnesium Oxide Nanostructures. *J. Phys. Chem. B* **2005**, *109*, 11204–11208. [[CrossRef](#)]
21. Kumari, L.; Li, W.Z.; Vannoy, C.H.; Leblanc, R.M.; Wang, D.Z. Synthesis, Characterization and Optical Properties of Mg(OH)₂ Micro-/Nanostructure and Its Conversion to MgO. *Ceram. Int.* **2009**, *35*, 3355–3364. [[CrossRef](#)]

22. Ouraipryvan, P.; Sreethawong, T.; Chavadej, S. Synthesis of Crystalline MgO Nanoparticle with Mesoporous-Assembled Structure via a Surfactant-Modified Sol–Gel Process. *Mater. Lett.* **2009**, *63*, 1862–1865. [[CrossRef](#)]
23. Bokov, D.; Turki Jalil, A.; Chupradit, S.; Suksatan, W.; Javed Ansari, M.; Shewael, I.H.; Valiev, G.H.; Kianfar, E. Nanomaterial by Sol-Gel Method: Synthesis and Application. *Adv. Mater. Sci. Eng.* **2021**, *2021*, 5102014. [[CrossRef](#)]
24. Tamilselvi, P.; Yelilarasi, A.; Hema, M.; Anbarasan, R. Synthesis of Hierarchical Structured MgO by Sol-Gel Method. *Nano Bull.* **2013**, *2*, 130106.
25. Devaraja, P.B.; Avadhani, D.N.; Prashantha, S.C.; Nagabhushana, H.; Sharma, S.C.; Nagabhushana, B.M.; Nagaswarupa, H.P. Synthesis, Structural and Luminescence Studies of Magnesium Oxide Nanopowder. *Spectrochim. Acta Part A Mol. Biomol. Spectrosc.* **2014**, *118*, 847–851. [[CrossRef](#)] [[PubMed](#)]
26. Ding, Y.; Zhang, G.; Wu, H.; Hai, B.; Wang, L.; Qian, Y. Nanoscale Magnesium Hydroxide and Magnesium Oxide Powders: Control Over Size, Shape, and Structure via Hydrothermal Synthesis. *Chem. Mater.* **2001**, *13*, 435–440. [[CrossRef](#)]
27. Selvam, N.C.S.; Kumar, R.T.; Kennedy, L.J.; Vijaya, J.J. Comparative Study of Microwave and Conventional Methods for the Preparation and Optical Properties of Novel MgO-Micro and Nano-Structures. *J. Alloys Compd.* **2011**, *509*, 9809–9815. [[CrossRef](#)]
28. Maurya, A.; Bhatia, N. Microwave Assisted Sol Gel Synthesis of Magnesium Oxide (MgO). *Int. J. Eng. Res. Dev.* **2017**, *13*, 1–6.
29. Makhluif, S.; Dror, R.; Nitzan, Y.; Abramovich, Y.; Jelinek, R.; Gedanken, A. Microwave-Assisted Synthesis of Nanocrystalline MgO and Its Use as a Bactericide. *Adv. Funct. Mater.* **2005**, *15*, 1708–1715. [[CrossRef](#)]
30. Gajengi, A.L.; Sasaki, T.; Bhanage, B.M. Mechanistic Aspects of Formation of MgO Nanoparticles under Microwave Irradiation and Its Catalytic Application. *Adv. Powder Technol.* **2017**, *28*, 1185–1192. [[CrossRef](#)]
31. Abinaya, S.; Kavitha, H.P. Magnesium Oxide Nanoparticles: Effective Antilarvicidal and Antibacterial Agents. *ACS Omega* **2023**, *8*, 5225–5233. [[CrossRef](#)]
32. Salman, K.D.; Abbas, H.H.; Aljawad, H.A. Synthesis and Characterization of MgO Nanoparticle via Microwave and Sol-Gel Methods. *J. Phys. Conf. Ser.* **2021**, *1973*, 012104. [[CrossRef](#)]
33. Bhargava, R.; Khan, S. Superior Dielectric Properties and Bandgap Modulation in Hydrothermally Grown Gr/MgO Nanocomposite. *Phys. Lett. A* **2019**, *383*, 1671–1676. [[CrossRef](#)]
34. Bhuvaneshwari, S.; Satheeskumar, S.; Velayutham, J.; Rahman, B.S. Hydrothermal Synthesis and Characterization of ZnO, MgO and ZnO/MgO Nanocomposites. *Rasayan J. Chem.* **2021**, *14*, 1581–1586. [[CrossRef](#)]
35. Gao, W.; Zhou, T.; Louis, B.; Wang, Q. Hydrothermal Fabrication of High Specific Surface Area Mesoporous MgO with Excellent CO₂ Adsorption Potential at Intermediate Temperatures. *Catalysts* **2017**, *7*, 116. [[CrossRef](#)]
36. Hadia, N.M.A.; Mohamed, H.A.-H. Characteristics and Optical Properties of MgO Nanowires Synthesized by Solvothermal Method. *Mater. Sci. Semicond. Process.* **2015**, *29*, 238–244. [[CrossRef](#)]
37. Kado, Y.; Soneda, Y. Capacitor Performance of MgO-Templated Carbons Synthesized Using Hydrothermally Treated MgO Particles. *Microporous Mesoporous Mater.* **2021**, *310*, 110646. [[CrossRef](#)]
38. Peng, W.; Li, J.; Chen, B.; Wang, N.; Luo, G.; Wei, F. Mesoporous MgO Synthesized by a Homogeneous-Hydrothermal Method and Its Catalytic Performance on Gas-Phase Acetone Condensation at Low Temperatures. *Catal. Commun.* **2016**, *74*, 39–42. [[CrossRef](#)]
39. Sutradhar, N.; Sinhamahapatra, A.; Pahari, S.K.; Pal, P.; Bajaj, H.C.; Mukhopadhyay, I.; Panda, A.B. Controlled Synthesis of Different Morphologies of MgO and Their Use as Solid Base Catalysts. *J. Phys. Chem. C* **2011**, *115*, 12308–12316. [[CrossRef](#)]
40. Zhao, X.; Ji, G.; Liu, W.; He, X.; Anthony, E.J.; Zhao, M. Mesoporous MgO Promoted with NaNO₃/NaNO₂ for Rapid and High-Capacity CO₂ Capture at Moderate Temperatures. *Chem. Eng. J.* **2018**, *332*, 216–226. [[CrossRef](#)]
41. Dercz, G.; Prusik, K.; Pająk, L.; Malinowski, J.J.; Pudło, W. Structure Studies on Nanocrystalline Powder of MgO Xerogel Prepared by Sol-Gel Method. *Mater. Sci.* **2009**, *27*, 201–207.
42. Mastuli, M.S.; Kamarulzaman, N.; Nawawi, M.A.; Mahat, A.M.; Rusdi, R.; Kamarudin, N. Growth Mechanisms of MgO Nanocrystals via a Sol-Gel Synthesis Using Different Complexing Agents. *Nanoscale Res. Lett.* **2014**, *9*, 134. [[CrossRef](#)]
43. Pei, L.-Z.; Yin, W.-Y.; Wang, J.-F.; Chen, J.; Fan, C.-G.; Zhang, Q.-F. Low Temperature Synthesis of Magnesium Oxide and Spinel Powders by a Sol-Gel Process. *Mater. Res.* **2010**, *13*, 339–343. [[CrossRef](#)]
44. Possato, L.G.; Gonçalves, R.G.L.; Santos, R.M.M.; Chaves, T.F.; Briois, V.; Pulcinelli, S.H.; Martins, L.; Santilli, C.V. Sol-Gel Synthesis of Nanocrystalline MgO and Its Application as Support in Ni/MgO Catalysts for Ethanol Steam Reforming. *Appl. Surf. Sci.* **2021**, *542*, 148744. [[CrossRef](#)]
45. Verma, R.; Naik, K.K.; Gangwar, J.; Srivastava, A.K. Morphology, Mechanism and Optical Properties of Nanometer-Sized MgO Synthesized via Facile Wet Chemical Method. *Mater. Chem. Phys.* **2014**, *148*, 1064–1070. [[CrossRef](#)]
46. Zieliński, M.; Czajka, B.; Pietrowski, M.; Tomska-Foralewska, I.; Alwin, E.; Kot, M.; Wojciechowska, M. MgO-MgF₂ System Obtained by Sol–Gel Method as an Immobilizing Agent of the Electrolyte Applied in the High Temperature Cells. *J. Sol-Gel Sci. Technol.* **2017**, *84*, 368–374. [[CrossRef](#)]
47. Yusoff, H.M.; Hazwani, N.U.; Hassan, N.; Izwani, F. Comparison of Sol Gel and Dehydration Magnesium Oxide (MgO) as a Catalyst in Michael Addition Reaction. *Int. J. Integr. Eng.* **2015**, *7*, 43–50.
48. Thommes, M.; Kaneko, K.; Neimark, A.V.; Olivier, J.P.; Rodriguez-Reinoso, F.; Rouquerol, J.; Sing, K.S.W. Physisorption of Gases, with Special Reference to the Evaluation of Surface Area and Pore Size Distribution (IUPAC Technical Report). *Pure Appl. Chem.* **2015**, *87*, 1051–1069. [[CrossRef](#)]

49. Pathak, N.; Ghosh, P.S.; Gupta, S.K.; Kadam, R.M.; Arya, A. Defects Induced Changes in the Electronic Structures of MgO and Their Correlation with the Optical Properties: A Special Case of Electron–Hole Recombination from the Conduction Band. *RSC Adv.* **2016**, *6*, 96398–96415. [[CrossRef](#)]
50. Duong, T.H.Y.; Nguyen, T.N.; Oanh, H.T.; Dang Thi, T.A.; Giang, L.N.T.; Phuong, H.T.; Anh, N.T.; Nguyen, B.M.; Tran Quang, V.; Le, G.T.; et al. Synthesis of Magnesium Oxide Nanoplates and Their Application in Nitrogen Dioxide and Sulfur Dioxide Adsorption. *J. Chem.* **2019**, *2019*, 4376429. [[CrossRef](#)]
51. Hazarika, R.; Kalita, B. Effect of Oxygen Vacancy Defects on Electronic and Optical Properties of MgO Monolayers: First Principles Study. *Mater. Sci. Eng. B* **2022**, *286*, 115974. [[CrossRef](#)]
52. Choudhury, B.; Basyach, P.; Choudhury, A. Monitoring F, F⁺ and F₂²⁺ Related Intense Defect Emissions from Nanocrystalline MgO. *J. Lumin.* **2014**, *149*, 280–286. [[CrossRef](#)]
53. Sellaiyan, S.; Uedono, A.; Sivaji, K.; Janet Priscilla, S.; Sivasankari, J.; Selvalakshmi, T. Vacancy Defects and Defect Clusters in Alkali Metal Ion-Doped MgO Nanocrystallites Studied by Positron Annihilation and Photoluminescence Spectroscopy. *Appl. Phys. A* **2016**, *122*, 920. [[CrossRef](#)]
54. Look, D.C. Recent Advances in ZnO Materials and Devices. *Mater. Sci. Eng. B* **2001**, *80*, 383–387. [[CrossRef](#)]
55. Vijaya Shanthy, R.; Kayalvizhi, R.; John Abel, M.; Neyvasagam, K. Analysis on the Combined Effect of Gd³⁺ and Er³⁺ Lanthanides in the Microscopic, Physicochemical and Photocatalytic Characteristics of MgO Nanoparticles. *Opt. Mater.* **2022**, *125*, 112118. [[CrossRef](#)]
56. Mageshwari, K.; Sathyamoorthy, R. Studies on Photocatalytic Performance of MgO Nanoparticles Prepared by Wet Chemical Method. *Trans. Indian Inst. Met.* **2012**, *65*, 49–55. [[CrossRef](#)]
57. Khan, M.I.; Akhtar, M.N.; Ashraf, N.; Najeeb, J.; Munir, H.; Awan, T.I.; Tahir, M.B.; Kabli, M.R. Green Synthesis of Magnesium Oxide Nanoparticles Using Dalbergia Sissoo Extract for Photocatalytic Activity and Antibacterial Efficacy. *Appl. Nanosci.* **2020**, *10*, 2351–2364. [[CrossRef](#)]
58. Collin, F. Chemical Basis of Reactive Oxygen Species Reactivity and Involvement in Neurodegenerative Diseases. *Int. J. Mol. Sci.* **2019**, *20*, 2407. [[CrossRef](#)]
59. Todan, L.; Dascalescu, T.; Preda, S.; Andronesco, C.; Munteanu, C.; Culita, D.C.; Rusu, A.; State, R.; Zaharescu, M. Porous Nanosized Oxide Powders in the MgO-TiO₂ Binary System Obtained by Sol-Gel Method. *Ceram. Int.* **2014**, *40*, 15693–15701. [[CrossRef](#)]

Disclaimer/Publisher’s Note: The statements, opinions and data contained in all publications are solely those of the individual author(s) and contributor(s) and not of MDPI and/or the editor(s). MDPI and/or the editor(s) disclaim responsibility for any injury to people or property resulting from any ideas, methods, instructions or products referred to in the content.